Isotopic constraints on ocean redox at the end of the Eocene

Journal Item

Earth and Planetary Science Letters 562 (2021) 116814

Contents lists available at ScienceDirect

Earth and Planetary Science Letters

www.elsevier.com/locate/epsl

Isotopic constraints on ocean redox at the end of the Eocene

Alexander J. Dickson [a,*], Marie-Laure Bagard [b,c], Joachim A.R. Katchinoff [d], Marc Davies [b,e], Simon W. Poulton [f], Anthony S. Cohen [b]

[a] Department of Earth Sciences, Royal Holloway University of London, Egham, Surrey, TW20 0EX, UK
[b] Department of Environment, Earth and Ecosystems, The Open University, Milton Keynes, MK7 6AA, UK
[c] Department of Earth Sciences, University of Cambridge, Downing Street, Cambridge, Cambridgeshire, CB2 3EQ, UK
[d] Department of Geology and Geophysics, Yale University, New Haven, CT, 06520-8109, USA
[e] School of Geography, Earth and Environmental Sciences, University of Plymouth, Plymouth, Devon, PL4 8AA, UK
[f] School of Earth and Environment, University of Leeds, Leeds, LS2 9JT, UK

ARTICLE INFO

Article history:
Received 28 October 2020
Received in revised form 30 January 2021
Accepted 7 February 2021
Available online xxxx
Editor: F. Moynier

Keywords:
molybdenum isotopes
uranium isotopes
redox
Para-Tethys
Eocene-Oligocene transition

ABSTRACT

A multi-million-year decrease in global temperatures during the Eocene was accompanied by large reorganisations to ocean circulation, ocean chemistry and biological productivity. These changes culminated in the rapid growth of grounded ice on Antarctica during the Eocene–Oligocene climate transition (EOT), ~34 million years ago. However, while it is likely that environmental perturbations of this magnitude altered the oceanic oxygen inventory, the sign and magnitude of the response is poorly constrained. We show that euxinic, hydrographically restricted conditions developed in the Austrian Molasse Basin during the EOT. The isotopic compositions of molybdenum and uranium captured by sediments accumulating in the Molasse Basin at this time reveal that the global extent of sulfidic conditions during the EOT was not appreciably different to that of the Early Eocene greenhouse world. Our results suggest that the early Cenozoic oceans were buffered against extreme long-term changes in oxygenation.

1. Introduction

The spread of deoxygenated zones in the modern ocean threatens the stability of marine ecosystems and nutrient cycling. Predicting the pattern of future deoxygenation trends is difficult because the key drivers – water temperature, organic matter production, and water mass ventilation – may interact with each other in non-linear ways over short and long timescales (Oschlies et al., 2018). In the early part of the Cenozoic Era, the Earth moved from a greenhouse world with temperatures ~10 °C warmer than pre-industrial during the early Eocene Climatic Optimum (EECO, ~50–53 Ma) (Cramwinckel et al., 2018; Zachos et al., 2008) to a glaciated world in the early Oligocene, with the inception of an extensive Antarctic ice sheet during the Eocene–Oligocene Transition (EOT, ~33.7 Ma) (Lear et al., 2008; Katz et al., 2008). This ~20-million-year climatic transition presents an opportunity to study how the main drivers of seawater oxygen concentration [O_2] interacted over multi-million year timescales.

Published data provide contradictory information about the direction and magnitude of early Cenozoic changes in seawater [O_2]. A long-term decline in deep-ocean temperatures from 53–34 Ma should have increased the [O_2] of global deepwaters due to the higher solubility of oxygen in colder water. The magnitude of this increase can be roughly estimated from the temperature declines inferred from TEX_{86}, Mg/Ca, $\delta^{18}O$ and pollen/spore assemblage proxy data at high northern (Eldrett et al., 2009) and southern (Bijl et al., 2009; Hollis et al., 2009; Liu et al., 2009) latitudes and from gas solubility coefficients, to ~0.5–3 ml/l (Weiss, 1970). High-latitude surface temperature changes are disproportionately important for deep-ocean [O_2] due to the formation of deepwaters that occupy a large volume of the ocean interior. Before ~50 Ma, deepwater production was concentrated in the Southern Ocean (Hohbein et al., 2012; Nunes and Norris, 2006) where early Cenozoic surface temperature decreases were particularly large (Bijl et al., 2009; Hollis et al., 2009; Liu et al., 2009).

The effect of declining temperatures on deepwater [O_2] would have been partly balanced by the remineralisation of exported organic matter into the ocean interior. However, organic matter export was spatially and temporally variable during the Eocene: during the EECO, high ocean temperatures and microbial metabolic rates enhanced the efficiency by which exported organic matter was recycled (Moore et al., 2008; Olivarez-Lyle and Lyle, 2006), possibly leading to lower deep ocean [O_2] than at present (Sexton et al., 2011). A second peak in organic matter export after ~37 Ma

* Corresponding author.
E-mail address: alex.dickson@rhul.ac.uk (A.J. Dickson).

https://doi.org/10.1016/j.epsl.2021.116814

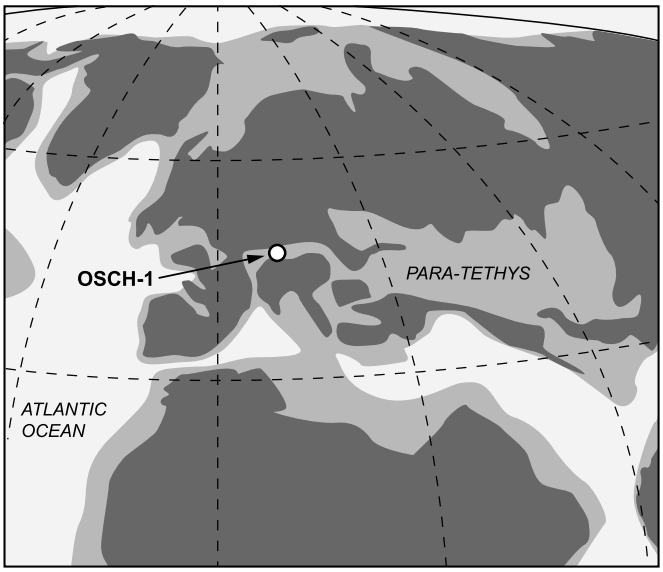

Fig. 1. Paleogeography of the European Para-Tethys in the Early Oligocene. The location of the Oberschauersberg-1 (OSCH-1) core in the Austrian Molasse Basin is indicated by the circle. Dark grey areas are landmasses, light grey areas are shallow marine shelves, and white areas are deeper marine areas.

has been attributed to a greater oceanic nutrient inventory and/or rapid ocean overturning (Diekmann et al., 2004; Diester-Haas and Zahn, 1996). The situation is further complicated by patterns of organic matter export in different ocean basins (Moore et al., 2008), temporal changes in the rate of ocean mixing after the EECO (Sexton et al., 2006) and changes in deep ocean ventilation linked to the onset of Northern Component Deepwater formation after ~49 Ma (Hohbein et al., 2012; Sexton et al., 2006). It is thus unclear how organic matter export would have balanced lower temperatures at a global scale to control net $[O_2]$.

Here we use Mo and U isotope compositions of shales deposited in the euxinic and partially restricted Molasse Basin (MB) to constrain global ocean oxygen distributions at the end of the long-term Eocene cooling trend. The MB was a tectonically controlled narrow seaway that formed north of the Alpine thrust belt as the European Plate was subducted beneath the Adriatic Plate during the Paleogene (Fig. 1). The regional tectonic context is described in detail by Sissingh (1997), Wagner (1998) and references therein. The sedimentary infill is Late-Eocene to Miocene in age and consists of a series of sandstones, limestones, marls and shales (Schulz et al., 2002; Sissingh, 1997). The basin was connected to the Tethys Ocean via a shallow strait to the Valence Basin in the southwest, and to the Para-Tethys Sea via shallow seaways to the north and east (Sissingh, 1997). We focus our study on the Oberschauersberg-1 (OSCH-1) core, in which organic-rich shales of the Eocene–Oligocene age Schöneck Fm are underlain by the Ampfing Sandstone and overlain by the Dynow Marl (Fig. 2). The OSCH-1 sedimentary succession is representative of the MB (Schulz et al., 2002, 2005) (Fig. S1).

2. Methods

2.1. Molybdenum and uranium isotopes

Molybdenum and uranium isotope measurements were performed at The Open University. Powdered mudrocks were accurately weighed and mixed with an aliquot of either a ^{97}Mo-^{100}Mo double spike or IRMM 3636 U double spike, aiming for a Mo_{spike}/Mo_{sample} of ~0.6 or a U_{spike}/U_{sample} of ~0.04. Samples were digested with 3 : 1 concentrated HNO_3 and HCl at 150 °C to dissolve the non-detrital fraction. Mo was separated from matrix elements with AG1-X8 anion exchange resin using protocols developed by Pearce et al. (2010), as modified by Dickson et al. (2016). Mo isotope ratios were measured in low resolution on a Thermo-Finnigan Neptune MC-ICP-MS, using a CETAC Aridus II desolvating nebulizer system for sample introduction, and fitted with nickel sample and H skimmer cones. Molybdenum isotope ratios are reported as the per mil deviation from a standard solution and calculated using the following equation:

$$\delta^{98}Mo = \left[\left(^{98}Mo/^{95}Mo_{sample}\right)/\left(^{98}Mo/^{95}Mo_{std}\right) - 1\right] * 1000$$

All Mo isotope data were determined relative to an in-house Mo solution standard (Fisher Chemicals, ICP Mo standard solution, lot 9920914-150). They have subsequently been normalised to NIST 3134, firstly using a −0.37‰ offset between the two standards (Goldberg et al., 2013), which was confirmed by repeated measurements of NIST 3134 relative to the OU standard over the measurement period (0.37±0.06‰, 2 S.D., n=70), and secondly by adding 0.25‰ following the recommendation of Nägler et al. (2015). External reproducibility of the measurements was assessed by repeatedly processing the USGS SDO-1 shale standard through the full chemical and analytical procedure, which yielded a δ^{98}Mo of 1.07±0.04‰ (2 S.D., n=16), similar to published values (Goldberg et al., 2013). Total procedural blanks measured by isotope dilution were negligible, between 1–4 ng.

U was purified from the sample matrix with established U chromatography protocols using UTEVA resin. $^{238}U/^{235}U$ ratios were measured in low resolution on a Thermo-Finnigan Neptune MC-ICP-MS, set up with nickel Jet sampler and X skimmer cones, and equipped with a CETAC Aridus II desolvating nebulizer system for sample introduction. Uranium isotope ratios are reported as the per mil deviation from CRM-112A standard:

$$\delta^{238}U = \left[\left(^{238}U/^{235}U_{sample}\right)/\left(^{238}U/^{235}U_{CRM112A}\right) - 1\right] * 1000$$

External reproducibility was assessed by measuring several standards repeatedly over the analytical period. The solution standard SRM 950A gives a δ^{238}U of 0.03±0.06‰ (n=82, 2 S.D.), similar to previously published values (Andersen et al., 2017). Measurements of seawater yielded a δ^{238}U value of −0.39±0.05‰ (n=8, 2 S.D.), similar to published values (−0.39±0.01‰ (Andersen et al., 2017)); USGS SDO-1 shale yielded a δ^{238}U of −0.09±0.06‰ (n=20, 2 S.D.), similar to published values (Tissot and Dauphas, 2015). Total procedural blanks measured by isotope dilution were 6–12 pg.

2.2. Osmium isotopes

Osmium isotopes were measured at Royal Holloway University of London. Sample powders were digested with a $^{190}Os/^{185}Re$ spike solution and 8 ml 3 : 1 HNO_3 and HCl in flame-sealed Carius tubes at 220 °C for 48 hours. After digestion, Os was purified by solvent extraction using $CHCl_3$ and concentrated hydrobromic acid (Cohen and Waters, 1996), followed by microdistillation in 2M H_2SO_4/CrO_3(VI) (Birck et al., 1997). Re was purified from the digested inverse aqua regia by solvent extraction into iso-amyl alcohol and back extraction into high-purity water (Birck et al., 1997).

Os solutions were loaded onto pre-cleaned and de-gassed high-purity Pt filaments and measured as osmium oxide species using peak-hopping on the axial SEM of an Isotopx Phoenix TIMS. Oxygen-corrected $^{187}Os/^{188}Os$ ratios were mass corrected to a $^{192}Os/^{188}Os$ ratio of 3.083 (Brandon et al., 2006) and blank-corrected. Accuracy and precision were monitored by measuring the DROsS standard (Luguet et al., 2008). $^{187}Os/^{188}Os$ ratios aver-

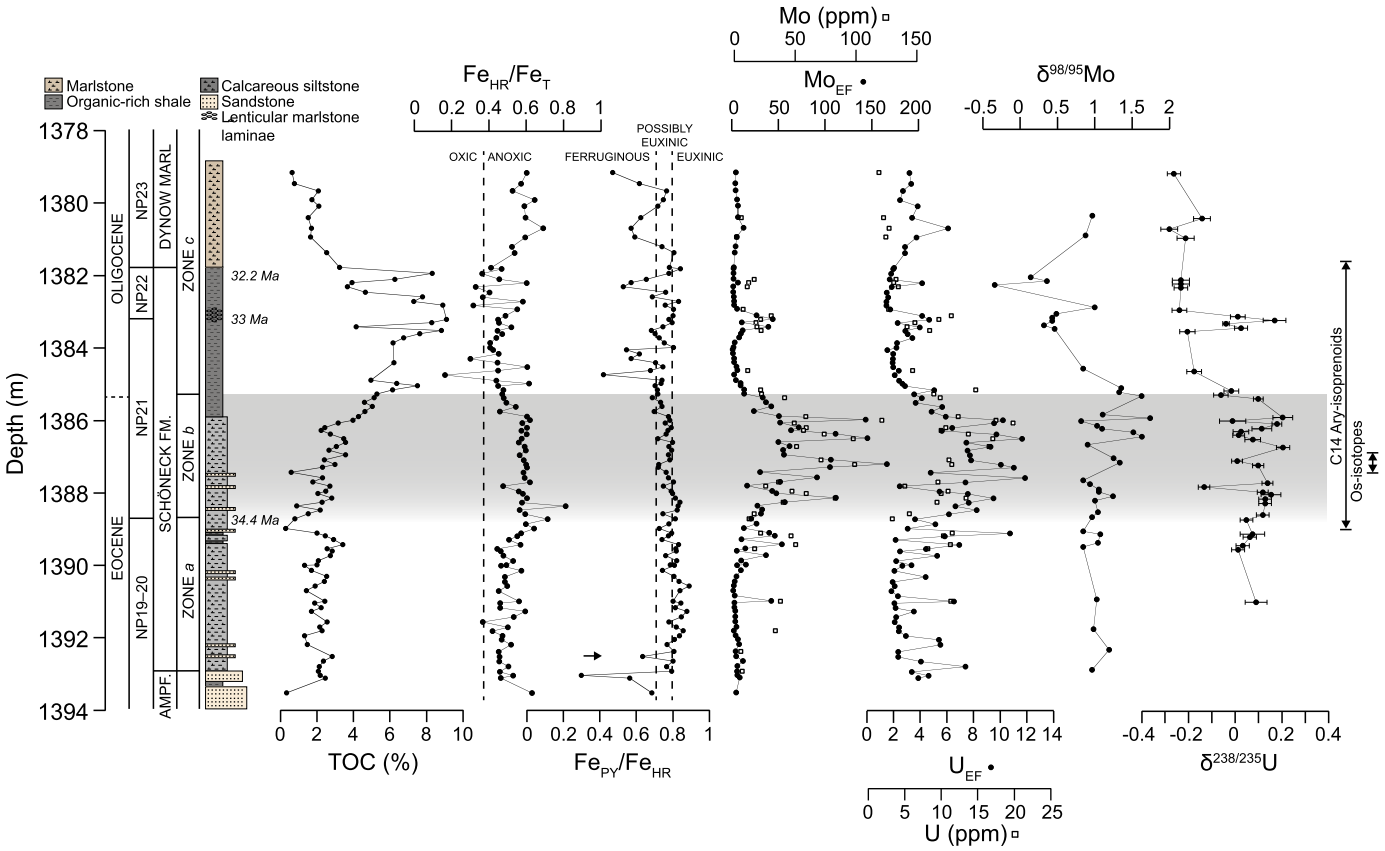

Fig. 2. Stratigraphy of the OSCH-1 core. All geochemical data are from this study. Nannofossil zones from the Fischlham-1 core were lithostratigraphically correlated to the OSCH-1 core by Schulz et al. (2002), with an approximate uncertainty of ~±1–2 m. The stratigraphic range of aryl-isoprenoids are from Schulz et al. (2002). The shaded region indicates the interval of elevated trace metal concentrations in the Molasse Basin during the EOT. Uncertainties for Mo-isotope data are smaller than the symbol size. The stratigraphic level at which Os-isotope analyses were undertaken is indicated; raw data are available in the Supplementary Information. Numerical ages are based on the calibrated timescale of ODP Site 1218 in Coxall and Wilson (2011) via transfer of the nannofossil zone boundaries.

aged 0.1601 compared to a reference value of 0.16092 (Nanne et al., 2017). Precision was ~2.3% over the course of this study (n=6). Os concentrations were calculated by isotope dilution using mass-bias corrected $^{190}Os/^{188}Os$ ratios. Procedural blanks were ~0.06 ± 0.07 pg (n=3, 1 S.D.) with an average $^{187}Os/^{188}Os$ ratio of 0.77.

Re solutions were measured as ~0.5 ppb solutions on a Neptune Plus MC-ICP-MS using a standard introduction system (wet plasma, SIS). To correct for instrumental mass fractionation, sample aliquots were doped with 10 ppb NIST 3636 to obtain a W/Re ratio of ~20. ^{185}Re, ^{187}Re, ^{184}W, ^{186}W and ^{189}Os were measured simultaneously using Faraday detectors equipped with 10^{11} resistors (W) and 10^{13} resistors (Re). $^{185}Re/^{187}Re$ ratios were corrected to a $^{186}W/^{184}W$ ratio of 0.92767 using an exponential mass bias law. Re concentrations were calculated by isotope dilution using corrected $^{185}Re/^{187}Re$ ratios. A small correction for ^{187}Os inference on ^{187}Re was made by monitoring ^{189}Os. For all samples, this correction was insignificant. External reproducibility for Re concentrations was estimated with separate digestions of well-characterised mudrock standard 00N118 (Dickson et al., 2015), yielding a concentration of 57.05 ppb ± 0.2% (2 S.D., n=5). Procedural blanks were insignificant (4.9 ± 0.9 pg, 2 S.D., n=3). The relative uncertainty on age-corrected $^{187}Os/^{188}Os_{(i)}$ ratios based on analyses of three 00N118 standards in the sample batches analysed for this study is ~1.9%.

2.3. Fe-speciation

Highly reactive non-sulfidized Fe pools were determined using well-established sequential leaching procedures at the University of Leeds (Poulton and Canfield, 2005), followed by concentration measurements using Atomic Adsorption Spectroscopy. Pyrite Fe was determined by chromous chloride distillation (Canfield et al., 1986). Replicate analyses gave a RSD of <5% for all extraction steps. Total Fe concentrations used to calculate Fe_{HR}/Fe_T ratios were determined by XRF.

2.4. Major elements

Major element oxides were measured by X-Ray Fluorescence (XRF) analysis at the University of Edinburgh School of GeoSciences using a Philips PW2404 wavelength dispersive XRF spectrometer. Elemental intensities were corrected for background and known peak overlap interferences, and medium-term instrumental drift was taken into account using a drift normalisation monitor. Calibration lines were produced from a large number of reference materials (ca. 20 for major elements) encompassing a wide range of silicate compositions. Accuracy and precision for most elements in the analysed rock standards are better than ±3% and 1% RSD respectively.

2.5. Minor elements

For trace element analysis by ICPMS, sample and standard rock powders were prepared in a clean room environment using Teflon-distilled reagents and ultra-pure water (18.2 MΩ). Rock powders were digested in 4 : 1 concentrated HF/HNO_3, dried and refluxed in 5 M HNO_3; these solutions were rinsed into a 125 ml polypropylene bottle and made up to 100 g with ultra-pure water. The

solutions were analysed at the Open University using a standard Agilent 7500 Series ICP-MS. The analyses were carried out in a single batch, including one rock-standard (USGS SDO-1), a procedural duplicate and a blank which were repeatedly analysed for blank and drift correction purposes. In addition, a minimum of six out of eight rock standards (including WS-E, W-2, DNC-1, JB-2, JB-3, BCR-2 BHVO-1 and BIR-1) were analysed to calibrate the instrument. Accuracy and precision, estimated from the repeat analyses of SDO-1, were better than 5% (2 RSD) for all elements.

2.6. Bulk organic geochemistry

%TOC was measured using a Rock Eval 6 at the University of Oxford following standard analytical protocols (Behar et al., 2001). Relative uncertainty on %TOC measurements was ~0.2%, assessed by repeated analyses of an in-house shale standard (SAB-1).

3. Results and discussion

3.1. Severity and timing of local redox conditions during the EOT

Mo and U are both redox-sensitive metals, whose burial increases in marine sediments as local conditions become anoxic and sulfidic and/or as their concentrations in seawater increase. Mo burial occurs due to water-column precipitation of Fe-Mo-S particulates as sulfate reduction leads to the accumulation of aqueous H_2S (Helz et al., 2011; Vorlicek et al., 2019), or by sorption to exported organic particulates (Dahl et al., 2017; Dickson et al., 2019; Tessin et al., 2019). U burial occurs by the organic or inorganic reduction of U(VI) to U(IV) within the sediment coupled to diffusion of U across the sediment-water interface (Andersen et al., 2017).

Our new data from the OSCH-1 core reveal an interval of major trace-metal burial that was triggered by the development of water-column euxinia in the MB. This interval clearly stands out when the trace metal stratigraphy is divided into three zones. In the lowest zone (*a*, Fig. 2) concentrations of the redox-sensitive metals Mo and U average ~14 µg/g and 8 µg/g respectively; in zone *b* they are much higher (61 µg/g and 14 µg/g); and in zone *c* they average 9 µg/g and 6 µg/g. Sedimentation rates, approximately estimated from nannofossil zone boundary ages transferred from ODP Site 1218 (Coxall and Wilson, 2011) (Figs. 2 and 3), vary by a factor of ~3, while La/Yb ratios indicate subtle changes in detrital sediment provenance that are probably linked to the tectonically driven evolution of the MB across the study period (Fig. S3). Importantly, however, detrital sediments have little to no effect on Mo and U trends: enrichment factors (EF) of Mo and U, calculated by normalising Mo/Al and U/Al ratios to Upper Continental Crust averages of 0.0000135 and 0.000027 respectively (Rudnick and Gao, 2003), follow the major trends in the raw concentrations (Fig. 2). In zone *b*, ~93–99% of the accumulated Mo and ~64–92% of the accumulated U is non-detrital. The low proportions of detrital Mo and U also means that the isotopic compositions of these elements discussed in section 3.2, particularly in zone *b*, are dominated by the non-detrital fraction.

Determining the cause of the large changes in trace metal burial throughout zones *a–c* requires us to independently constrain local redox conditions and/or local seawater concentrations. To constrain local redox conditions, we use the Fe-speciation proxy that quantifies the amount of highly reactive (Fe_{HR}) and pyritised (Fe_{PY}) iron in sediments as a fraction of the total Fe (Fe_T) inventory (Raiswell et al., 2018) (Fig. 2). Sediments in zones *a–c* have consistently high Fe_{HR}/Fe_T ratios >0.38, signifying an anoxic depositional environment. Fe_{PY}/Fe_{HR} ratios are mostly >0.7, suggestive of euxinic conditions with H_2S present in the water column. In zone *a*, however, low Mo concentrations, pyrite framboids >4.5 µm with wide size distributions, and the minor presence of glauconite grains (Schulz et al., 2002) suggest that the high Fe_{PY}/Fe_{HR} ratios probably represent extensive diagenetic pyritization, with sulfidic conditions dominantly limited to sediment porewaters. In zone *c*, Fe_{PY}/Fe_{HR} ratios frequently decrease below ~0.7, signifying ferruginous (sulfur-limited) conditions. When viewed in context with low sterane/hopane ratios and high C_{org}/S ratios (Schulz et al., 2002, 2005), our new Fe-speciation data indicate that deposition in zone *c* probably occurred in a low-salinity setting due to a combination of relative sea-level fall and infill of shallow seaways to the north (Rögl, 1999). We conclude that from zones *a–b* the increase in trace-metal concentrations in the OSCH-1 core is related to the development of basinal euxinia, while the diminished trace-metal concentrations passing from zone *b* to *c* is linked to a declining local seawater inventory as the MB became isolated from the open ocean. The presence of aryl-isoprenoids from the base of zone *b* (Schulz et al., 2002, 2005) (Fig. 2) demonstrates that the local chemocline rose into the photic zone from this time, probably with higher aqueous H_2S concentrations that facilitated conversion of MoO_4- to particle-reactive thiomolybdates $MoO_{(4-x)}S_{(x)}^{2-}$ (Helz et al., 2011; Vorlicek et al., 2019). Mo removal may have been accelerated by better preservation of sinking organic matter under locally stagnant conditions.

We can tie the increase in Mo and U concentrations observed in the MB during zone *b* to the EOT, when the mass of grounded ice on Antarctica increased over a period of ~600 kyrs (Coxall and Wilson, 2011) (Fig. 3). In ODP Site 1218 in the Central Pacific Ocean, the nannofossil NP20/21 zonal boundary occurs below the initial increase in benthic foraminifera $\delta^{18}O$ that defines the first pulse of the EOT, and the NP21/22 zonal boundary occurs above the peak of the second increase in $\delta^{18}O$ that marks end of the EOT (Coxall and Wilson, 2011). Zone *b* in the OSCH-1 core is contained entirely within zone NP21 (Schulz et al., 2002). The biostratigraphic correlation is supported by our new $^{187}Os/^{188}Os_{(i)}$ measurements from zone *b* in the OSCH-1 core that range from 0.26–0.48 (Table S1). The Late Eocene features a unique global minimum in seawater $^{187}Os/^{188}Os$ of 0.22–0.28 that can be thus employed as a chemostratigraphic marker to tie the OSCH-1 core stratigraphy to the period of time immediately prior to the EOT (Ravizza and Paquay, 2008; Ravizza and Peucker-Ehrenbrink, 2003) (Fig. 3). The position of the Eocene/Oligocene boundary in the OSCH-1 core is not exact, and is approximately placed at the lithostratigraphic boundary between zones *a* and *b*.

Local tectonics preconditioned the MB to the development of local euxinia over timescales of millions of years (Schulz et al., 2002; Sissingh, 1997; Wagner, 1998). However, the correspondence in timing between the start of zone *b* and the EOT suggests that the ~70 m of eustatic sea-level fall associated with polar glaciation (Lear et al., 2008; Katz et al., 2008) may have been the final trigger for the short, intense period of euxinia that developed in the MB. Sea-level fall would have significantly reduced the transfer of water across shallow sills (Schulz et al., 2005) into a basin that was probably only ~400–800 m deep in the late Eocene (Schulz et al., 2002; Sissingh, 1997). Importantly, by triggering euxinia, sea-level fall may have initiated a feedback of regionally enhanced organic matter burial that contributed to pCO_2 decline across the EOT (Cramwinckel et al., 2018; Pearson et al., 2009). Age-equivalent organic-rich shales occur throughout the inter-connected basins of the Para-Tethys (Veto, 1987), suggesting that the depositional conditions documented in the OSCH-1 core were regionally extensive.

It has been shown that several species of planktonic foraminifera and coccolithophores adapted to oligotrophic conditions went extinct during the EOT, while species adapted to more eutrophic conditions became established (Dunkley-Jones et al., 2008; Pearson et al., 2008; Wade and Pearson, 2008). It is possible that nutri-

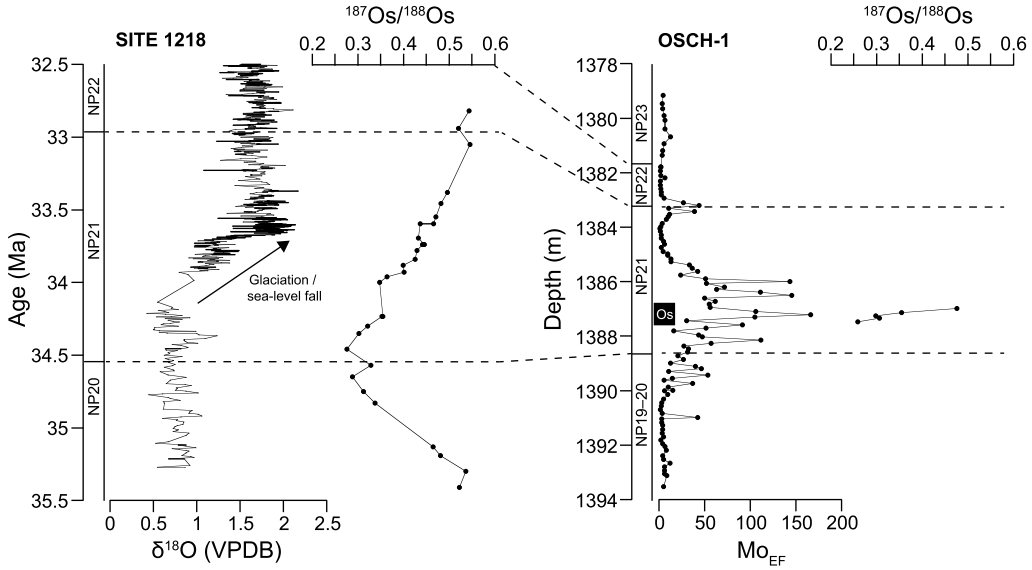

Fig. 3. Correlation of the OSCH-1 core to ODP Site 1218. Site 1218 oxygen isotope data are from Coxall and Wilson (2011) and osmium isotope data are from Dalai et al. (2006). Osmium isotope and Mo data from OSCH-1 are from this study. Correlation lines are placed at nannofossil zonal boundaries.

ent recycling in anoxic regions of the Para-Tethys, particularly of reactive P, may have contributed to the 'nutrification' of the surface ocean during the EOT. However, the importance of nutrient regeneration on open ocean biota compared to nutrient input from terrestrial weathering would depend on the degree of P export from the Para-Tethys, something that may be investigated in future.

3.2. Global redox conditions during the EOT

The development of locally euxinic conditions during the EOT in the MB in zone *b* allows us to use the isotopic compositions of Mo (δ^{98}Mo) and U (δ^{238}U) to constrain the global signature of anoxia and euxinia in the world's oceans at the end of the long-term Eocene cooling interval. The sedimentary compositions of Mo and U in settings such as these can be related directly to the isotopic compositions of these metals in the open ocean, acting as 'yardsticks' of global seawater chemistry (Andersen et al., 2017; Dickson, 2017).

Molybdenum and uranium are long-lived elements in the oceans, with residence times on the order of ~400,000–500,000 years (Dunk et al., 2002; Miller et al., 2011). A large fraction of the global burial flux of Mo occurs into oxic sediments containing Mn and Fe oxyhydroxides, with isotopic compositions that are generally lower than weathering input fluxes of ~0.6‰ (Kendall et al., 2017). In sulfidic settings, Mo burial occurs as thiomolybdate species or by adsorption to organic matter (Helz et al., 2011; Dahl et al., 2017; Dickson et al., 2019) with isotopic compositions higher than weathering inputs. The global burial flux of isotopically light Mo thus leverages the global seawater composition to a high value of ~2.3‰ today (Nakagawa et al., 2012; Goldberg et al., 2013). In situations where the oxic burial flux contracts at the expense of the burial of Mo into sulfidic sediments – such as during times when oceanic deoxygenation becomes more extensive – the seawater δ^{98}Mo would become lower. Sediments deposited in highly sulfidic water columns, with restricted water mass ventilation, have δ^{98}Mo compositions close to open-ocean seawater, due to its near-quantitative removal from the water column (Brüske et al., 2019; Neubert et al., 2008; Noordmann et al., 2015). For U isotopes, the seawater composition (today ~−0.4‰ (Tissot and Dauphas, 2015)) is largely controlled by the burial of U(IV) following biotic or abiotic reduction of U(VI) at the sediment-water interface (Andersen et al., 2017). This U(IV) burial flux has an effective isotopic composition that is ~0.6‰ higher than seawater, but the exact sediment-seawater difference depends on the diffusion and reduction rates and the overlying seawater composition (Andersen et al., 2014). Thus, at times of expanded oceanic deoxygenation and increased burial of U(IV), the isotopic composition of U in seawater becomes lower (Andersen et al., 2014, 2017; Tissot and Dauphas, 2015).

In zone *b*, where Fe-speciation data and the presence of aryl-isoprenoids indicate persistently euxinic conditions, δ^{98}Mo values are highest (1.6–1.8‰), and thus closest to the global seawater value (Fig. 2, Fig. S2). In zone *a*, δ^{98}Mo values of ~1.0‰ are probably fractionated from basin seawater under weakly sulfidic conditions. In zone *c*, low and variable δ^{98}Mo values (−0.4–1.0‰) were probably sensitized to local weathering inputs and sequestration pathways, in view of evidence for low salinity conditions and very low Mo concentrations.

We argue that the δ^{98}Mo fluctuations in zone *b* are related to changes in the fractional removal of Mo from MB seawater. In this zone, euxinic conditions, as recorded by Fe-speciation, persist throughout intervals of both low (~1.0‰) *and* high (~1.7‰) δ^{98}Mo values, thus limiting the effect of redox-driven changes to Mo cycling; δ^{98}Mo increases in tandem with [Mo], which suggests rapid conversion and burial of Mo as MoS_4^{2-} at higher [H_2S]. Maxima in δ^{98}Mo occur higher up-section in concert with increasing concentrations of aryl-isoprenoids, a trend that is suggestive of a shoaling chemocline and euxinic conditions spanning a larger fraction of the water column. Particulate shuttling cannot fully explain the fluctuations of δ^{98}Mo in zone *b*, because it would tend to lower δ^{98}Mo at times of higher [Mo] by delivering oxyhydroxide-adsorbed Mo to the seafloor, which is opposite to what we observe.

An important line of evidence for the drawdown of dissolved Mo in the MB during zone *b* comes from the inverse correlation between δ^{98}Mo and δ^{238}U (Fig. 4). This relationship emerges in restricted marine basins where the burial of isotopically heavy U(IV) outpaces U resupply by seawater exchange, causing the local basin water δ^{238}U to become lighter (Andersen et al., 2018; Brüske et al., 2019; Bura-Nakic et al., 2018). As the drawdown of Mo and U progresses, the isotopic compositions of the sediments evolve towards the seawater endmember, i.e. δ^{238}U becomes lower and δ^{98}Mo becomes higher. δ^{98}Mo and δ^{238}U are only inversely corre-

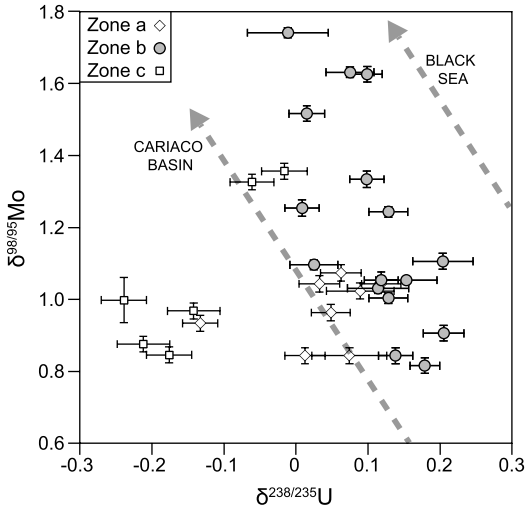

Fig. 4. Relationship between δ^{98}Mo and δ^{238}U. The inverse relationship for zone *b* is typical for marine basins where the U and Mo inventories of the local seawater are reduced because of trace metal burial in anoxic/euxinic conditions with limited seawater replenishment (Brüske et al., 2019; Bura-Nakic et al., 2018; Andersen et al., 2018). δ^{98}Mo versus δ^{238}U gradients are shown for recent sediments accumulating in the Black Sea and Cariaco Basin (dashed lines, from Brüske et al., 2019).

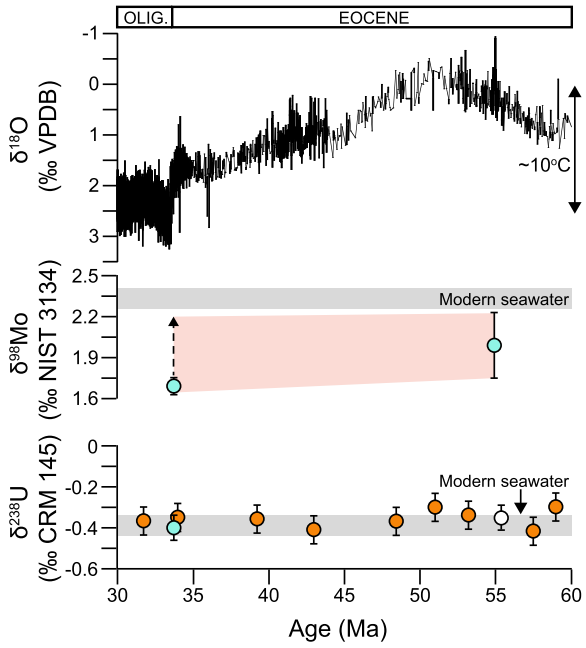

Fig. 5. Evolution of seawater δ^{98}Mo and δ^{238}U across the Early Cenozoic cooling interval (~53–33 Ma). Shale data are shown in blue (this study, Dickson et al., 2012; Dickson and Cohen, 2012), Fe-Mn crust data in orange (Wang et al., 2016) and carbonate data in white (Clarkson et al., 2021). The uncertainty in δ^{98}Mo of the Early Eocene data is the 2 S.D. range of values measured at the peak of the Paleocene–Eocene Thermal Maximum and Eocene Thermal Maximum 2, when basin euxinia was most pronounced. The uncertainty in δ^{98}Mo for the EOT data is the analytical uncertainty around the highest value measured, when trace metal drawdown was most pronounced. The vertical dashed line for the EOT data is the ~0.5‰ offset between modern Cariaco Basin sediments and seawater and indicates the highest possible value for Paleogene seawater δ^{98}Mo. Data from Wang et al. (2016) have been systematically corrected by +0.24‰, the difference between modern crust δ^{238}U and seawater δ^{238}U. The δ^{98}Mo and δ^{238}U of modern seawater are shown for comparison as horizontal grey bars. (For interpretation of the colours in the figure, the reader is referred to the web version of this article.)

lated in zone *b*, suggesting that in zone *a*, isotopic compositions are controlled by redox processes and in zone *c* by mixing with local weathering fluxes. Thus the Mo-U covariation trend supports the idea that the highest δ^{98}Mo compositions in zone *b* (~1.75‰) must have been close to the global seawater composition during the EOT due to basin drawdown. The slope of the correlation between δ^{98}Mo and δ^{238}U is close to that seen for the modern Cariaco Basin (Fig. 4). Given that the highest sediment δ^{98}Mo values in the Cariaco Basin are fractionated from global seawater by ~0.5‰ (Brüske et al., 2019), seawater during the EOT could have been as high as ~2.2‰ (Fig. 5). The highest δ^{238}U values in zone *b* sediments (~0.20‰) constrain the seawater δ^{238}U during the EOT to ~−0.40‰, assuming an effective fractionation from seawater of ~0.6‰ (Andersen et al., 2014, 2017; Brüske et al., 2019; Bura-Nakic et al., 2018). This value is close to the modern seawater value and is indistinguishable from estimates obtained from EOT-age Fe-Mn crusts (Wang et al., 2016) and from carbonates deposited in the Early Eocene (Clarkson et al., 2021).

The global seawater δ^{98}Mo composition for the Early Eocene (~56–54 Ma) has been estimated as 1.94±0.24‰ from sediments deposited in the Arctic Ocean (Dickson et al., 2012; Dickson and Cohen, 2012). This value is thought to capture the prevailing redox state of the Early Eocene global ocean as conditions for the quantitative removal of Mo became briefly established in the Arctic Ocean during the Paleocene–Eocene Thermal Maximum (~56 Ma) and Eocene Thermal Maximum 2 (~54 Ma) (Dickson and Cohen, 2012). This value characterizes the global redox state of the oceans slightly before the peak of Early Eocene warmth, and equates to a slightly larger fraction of the global seafloor being anoxic and sulfidic than today (Dickson, 2017). Our inferred range of global seawater δ^{98}Mo for the EOT (~1.7–2.2‰) overlaps this value (Fig. 5).

δ^{238}U values likewise vary little from the early Eocene to the EOT, as recorded by pelagic carbonates (Clarkson et al., 2021), Fe-Mn crusts (Wang et al., 2016) and shales (this study). The correspondence of all three sedimentary archives (carbonates, crusts, shales) is a powerful indication of the robustness of the observations (Fig. 5). Taken at face value, our observations indicate that the extent of anoxic and sulfidic conditions on the global seafloor was insensitive to the long-term changes in global climate and ocean circulation that occurred during the middle–late Eocene. We note however that the area of seafloor anoxia may fluctuate ~3–10 fold even within the uncertainties of the δ^{238}U method (Wang et al., 2016; Clarkson et al., 2021) and a similar magnitude of change might also be expected for the area of sulfidic deposition within the uncertainties of δ^{98}Mo. These uncertainties leave room for smaller long-term changes in whole-ocean redox that would be unresolvable by these methods.

3.3. Response of global ocean redox to long-term cooling

Wang et al. (2016) concluded that the invariance of low-resolution Fe-Mn crust δ^{238}U across Early Cenozoic cooling interval probably reflects an increase in oxygen consumption in the open ocean that balanced an expected increase in O_2 solubility at lower temperatures. While increases in biogenic silica export rates in the Southern Ocean at ~36–38 Ma are consistent with this suggestion (Diekmann et al., 2004; Diester-Haas and Zahn, 1996), biogenic silica export rates *decreased* sharply at approximately the same time in the equatorial Pacific Ocean (Moore et al., 2008). It is therefore not straightforward to invoke a whole-ocean change in organic matter export to explain the near-constancy of the δ^{238}U or δ^{98}Mo signatures across this interval. We suggest that the expansion of anoxic depositional conditions documented in the MB during the EOT, and perhaps in the wider Para-Tethys Sea (Veto, 1987), may have partly balanced any increase in U and Mo burial into more oxygenated sediments in the open ocean.

The response of global oxygenation to short-term environmental triggers has been studied for brief hyperthermal events such as the PETM (Dickson et al., 2012; Clarkson et al., 2021) and Creta-

ceous Oceanic Anoxic Events such as OAE 2 (Jenkyns, 2010; Poulton et al., 2015). The response of global ocean oxygenation to long-term environmental gradients is considerably less well-known. The apparent stability in seafloor redox conditions across the multi-million-year Early Cenozoic cooling interval, constrained by both δ^{98}Mo (this study) and δ^{238}U (this study, Wang et al., 2016), suggests that the oceans may be insensitive to extreme long-term changes in oxygenation. This insensitivity probably stems from the non-linear interaction of different Earth System feedbacks and processes (tectonics, ocean circulation, biogenic productivity, temperature) operating over timescales of 10^{3-6} years.

4. Conclusions

We present a detailed, multi-proxy study of the MB sedimentary succession that spans the EOT. New Os isotope data refine existing biostratigraphic constraints on the age of the deposits and demonstrate that an interval of basin euxinia developed during the EOT. We do not question that large-scale tectonics associated with the Alpine thrust belt preconditioned the basin to these depositional conditions but suggest that sea-level fall associated with polar glaciation may have tipped the balance in favour of hydrographic restriction and the accumulation of H_2S in the MB water column. These conditions are suitable for the application of redox-sensitive isotope systems to constrain global-scale redox conditions in the oceans. Mo and U isotope compositions of the sedimentary deposits in the OSCH-1 core negatively co-vary in the interval of euxinic deposition, supporting a model of metal drawdown from the basin seawater. The sediments can thus be used to place constraints on the seawater isotope compositions of these elements at ~34 Ma, which are indistinguishable from similar estimates for the Early Eocene (~54–56 Ma), prior to the commencement of long-term global cooling. Our data imply that the long-term Eocene cooling trend did not result in large-scale changes in the distribution of anoxic and sulfidic conditions on the global seafloor. We note, however, that the uncertainties associated with estimating seawater δ^{98}Mo signatures in particular are still significant enough to encourage future refinement to these observations.

CRediT authorship contribution statement

Alexander J. Dickson: Conceptualization, Funding acquisition, Investigation, Methodology, Project administration, Supervision, Visualization, Writing – original draft. **Marie-Laure Bagard:** Investigation, Methodology, Project administration, Supervision, Validation, Writing – review & editing. **Joachim A.R. Katchinoff:** Investigation, Writing – review & editing. **Marc Davies:** Investigation, Project administration, Supervision, Writing – review & editing. **Simon W. Poulton:** Funding acquisition, Investigation, Project administration, Supervision, Writing – review & editing. **Anthony S. Cohen:** Conceptualization, Funding acquisition, Project administration, Supervision, Writing – review & editing.

Declaration of competing interest

The authors declare that they have no known competing financial interests or personal relationships that could have appeared to influence the work reported in this paper.

Acknowledgements

We thank Samantha Hammond and Nisha Panchal for assistance with ICP-MS analyses, Nicholas Odling (University of Edinburgh) for XRF analyses and Rohöl-Aufsuchungs Aktiengesellschaft (RAG) for allowing us to sample their exploration cores in Pettenbach, Austria. This work was supported by the Natural Environment Research Council (NE/K006223/1). SWP acknowledges support from a Royal Society Wolfson Research Merit Award. Data are available as supplementary data tables and are archived in the Pangaea database (www.pangaea.de).

Appendix A. Supplementary material

Supplementary material related to this article can be found online at https://doi.org/10.1016/j.epsl.2021.116814.

References

Andersen, M.B., Matthews, A., Vance, D., Bar-Matthews, M., Archer, C., de Souza, G.F., 2018. A 10-fold decline in the deep Eastern Mediterranean thermohaline overturning circulation during the last interglacial period. Earth Planet. Sci. Lett. 503, 58–67.

Andersen, M.B., Romaniello, S., Vance, D., Little, S.H., Herdman, R., Lyons, T.W., 2014. A modern framework for the interpretation of $^{238}U/^{235}U$ in studies of ancient ocean redox. Earth Planet. Sci. Lett. 400, 184–194.

Andersen, M.B., Stirling, C.H., Weyer, S., 2017. Uranium isotope fractionation. Rev. Mineral. Geochem. 82, 799–850.

Behar, F., Beaumont, V., de B. Penteado, H.L., 2001. Rock-Eval 6 technology: performances and developments. Oil Gas Sci. Technol. 56, 111–134.

Bijl, P.K., Schouten, S., Sluijs, A., Reichart, G-J., Zachos, J.C., Brinkhuis, H., 2009. Early Palaeogene temperature evolution of the southwest Pacific Ocean. Nature 461, 776–779.

Birck, J.L., Roy Barman, M., Capmas, F., 1997. Re-Os isotopic measurements at the femtomole level in natural samples. Geostand. Newsl. 20, 19–27.

Brandon, A.D., Walker, R.J., Puchtel, I.S., 2006. Platinum-osmium isotope evolution of the Earth's mantle: constraints from chondrites and Os-rich alloys. Geochim. Cosmochim. Acta 70, 2093–2103.

Brüske, A., Weyer, S., Zhao, M-Y., Planavsky, N.J., Wegworth, A., Neubert, N., Dellwig, O., Lau, K.V., Lyons, T.W., 2019. Correlated molybdenum and uranium isotope signatures in modern anoxic sediments: implications for their use as paleo-redox proxy. Geochim. Cosmochim. Acta. https://doi.org/10.1016/j.gca.2019.11.031.

Bura-Nakic, E., Andersen, M.B., Archer, C., de Souza, G.F., Margus, M., Vance, D., 2018. Coupled Mo-U abundances and isotopes in a small marine euxinic basin: constraints on processes in euxinic basins. Geochim. Cosmochim. Acta 222, 212–229.

Canfield, D.E., Raiswell, R., Westrich, J.T., Reaves, C.M., Berner, R.A., 1986. The use of chromium reduction in the analysis of reduced inorganic sulfur in sediments and shales. Chem. Geol. 54, 149–155.

Clarkson, M.O., Lenton, T.M., Andersen, M.B., Bagard, M-L., Dickson, A.J., Vance, D., 2021. Upper limits on the extent of seafloor anoxia during the PETM from uranium isotopes and a biogeochemical model. Nat. Commun. 12, 399.

Cohen, A.S., Waters, F.G., 1996. Separation of osmium from geological materials by solvent extraction for analysis by thermal ionisation mass spectrometry. Anal. Chim. Acta 332, 267–275.

Coxall, H.K., Wilson, P.A., 2011. Early Oligocene glaciation and productivity in the eastern equatorial Pacific: insights into global carbon cycling. Paleoceanography 26, PA2221. https://doi.org/10.1029/2010PA002021.

Cramwinckel, M.J., Huber, M., Kocken, I.J., Agnini, C., Bijl, P.K., Bohaty, S.M., Frieling, J., Goldner, A., Hilgen, F.J., Kip, E.L., Peterse, F., van der Ploeg, R., Röhl, U., Schouten, S., Sluijs, A., 2018. Synchronous tropical and polar temperature evolution in the Eocene. Nature 559, 382–386.

Dahl, T.W., Chappaz, A., Hoek, J., McKenzie, C.J., Svane, S., Canfield, D.E., 2017. Evidence of molybdenum association with particulate organic matter under sulfidic conditions. Geobiology 15, 311–323.

Dalai, T.K., Ravizza, G.E., Peucker-Ehrenbrink, B., 2006. The Late Eocene 187Os/188Os excursion: chemostratigraphy, cosmic dust flux and the Early Oligocene glaciation. Earth Planet. Sci. Lett. 241, 477–492.

Dickson, A.J., 2017. A molybdenum isotope perspective on Phanerozoic deoxygenation events. Nat. Geosci. 10, 721–726.

Dickson, A.J., Cohen, A.S., 2012. A molybdenum isotope record of Eocene Thermal Maximum 2: implications for global ocean redox during the early Eocene. Paleoceanogr. Paleoclimatol. 27, PA3230. https://doi.org/10.1029/2012PA002346.

Dickson, A.J., Cohen, A.S., Coe, A.L., 2012. Seawater oxygenation during the Paleocene–Eocene Thermal Maximum. Geology 40, 639–642.

Dickson, A.J., Cohen, A.S., Coe, A.L., Davies, M., Shcherbinina, E.A., Gavrilov, Y.O., 2015. Evidence for weathering and volcanism during the PETM from Arctic Ocean and Peri-Tethys osmium isotope records. Palaeogeogr. Palaeoclimatol. Palaeoecol. 438, 300–307.

Dickson, A.J., Idiz, E., Porcelli, D., van den Boorn, S.H.J.M., 2019. The influence of thermal maturity on the stable isotope compositions and concentrations of

molybdenum, zinc and cadmium in organic-rich marine mudrocks. Geochim. Cosmochim. Acta 287, 205–220.
Dickson, A.J., Jenkyns, H.C., Porcelli, D., van den Boorn, S., Idiz, E., 2016. Basin-scale controls on the molybdenum-isotope composition of seawater during Oceanic Anoxic Event 2 (Late Cretaceous). Geochim. Cosmochim. Acta 178, 291–306.
Diekmann, B., Kuhn, G., Gersonde, R., Mackensen, A., 2004. Middle Eocene to early Miocene environmental changes in the sub-Antarctic Southern Ocean: evidence from biogenic and terrigenous depositional patterns at ODP Site 1090. Glob. Planet. Change 40, 295–313.
Diester-Haas, L., Zahn, R., 1996. Eocene–Oligocene transition in the Southern Ocean: history of water mass circulation and biological productivity. Geology 24, 163–166.
Dunk, R., Mills, R., Jenkins, W., 2002. A re-evaluation of the oceanic uranium budget for the Holocene. Chem. Geol. 190, 45–67.
Dunkley-Jones, T., Bown, P.R., Pearson, P.N., Wade, B.S., Coxall, H.K., Lear, C.H., 2008. Major shifts in calcareous phytoplankton assemblages through the Eocene–Oligocene transition of Tanzania and their implications for low-latitude primary productivity. Paleoceanogr. Paleoclimatol. 23, PA4204. https://doi.org/10.1029/2008PA001640.
Eldrett, J.S., Greenwood, D.R., Harding, I.C., Huber, M., 2009. Increased seasonality through the Eocene to Oligocene transition in northern high latitudes. Nature 459, 969–973.
Goldberg, T., Gordon, G.W., Izon, G., Archer, C., Pearce, C.R., McManus, J., Anbar, A.D., Rehkämper, M., 2013. Resolution of inter-laboratory discrepancies in Mo isotope data: an intercalibration. J. Anal. At. Spectrom. 28, 724–735.
Helz, G.R., Bura-Nakić, E., Mikac, N., Ciglenečki, I., 2011. New model for molybdenum behavior in euxinic waters. Chem. Geol. 284, 323–332.
Hohbein, M.W., Sexton, P.F., Cartwright, J.A., 2012. Onset of North Atlantic deep water production coincident with inception of the Cenozoic global cooling trend. Geology 40, 255–258.
Hollis, C.J., Handley, L., Crouch, E.M., Morgans, H.E.G., Baker, J.A., Creech, J., Collins, K.S., Gibbs, S.J., Huber, M., Schouten, S., Zachos, J.C., Pancost, R.D., 2009. Tropical sea temperatures in the high-latitude South Pacific during the Eocene. Geology 37, 99–102.
Jenkyns, H.C., 2010. Geochemistry of oceanic anoxic events. Geochem. Geophys. Geosyst. 11, Q03004. https://doi.org/10.1029/2009GC002788.
Katz, M.E., Miller, K.G., Wright, J.D., Wade, B.S., Browning, J.V., Cramer, B.S., Rosenthal, Y., 2008. Stepwise transition from the Eocene greenhouse to the Oligocene icehouse. Nat. Geosci. 1, 329–334.
Kendall, B., Dahl, T.W., Anbar, A.D., 2017. The stable isotope geochemistry of molybdenum. Rev. Mineral. Geochem. 82, 683–732.
Lear, C.H., Bailey, T.R., Pearson, P.N., Coxall, H.K., Rosenthal, Y., 2008. Cooling and ice growth across the Eocene–Oligocene transition. Geology 36, 251–254.
Liu, Z., Pagani, M., Zinniker, D., DeConto, R., Huber, M., Brinkhuis, H., Shah, S.R., Leckie, M., Pearson, A., 2009. Global cooling during the Eocene–Oligocene boundary. Science 323, 1187–1190.
Luguet, A., Nowell, G.M., Pearson, D.G., 2008. $^{184}Os/^{188}Os$ and $^{186}Os/^{188}Os$ measurements by Negative Thermal Ionisation Mass Spectrometry (N-TIMS): effects of interfering element and mass fractionation corrections on data accuracy and precision. Chem. Geol. 248, 342–362.
Miller, C.A., Peucker-Ehrenbrink, B., Walker, B.D., Marcantonio, F., 2011. Re-assessing the surface cycling of molybdenum and rhenium. Geochim. Cosmochim. Acta 75, 7146–7179.
Moore Jr., T.C., Jarrard, R.D., Olivarez Lyle, A., Lyle, M., 2008. Eocene biogenic silica accumulation rates at the Pacific equatorial divergence zone. Paleoceanogr. Paleoclimatol. 23. https://doi.org/10.1029/2007PA001514.
Nägler, T.F., Anbar, A.D., Archer, C., Goldberg, T., Gordon, G.W., Greber, N.D., Siebert, C., Sohrin, Y., Vance, D., 2015. Proposal for an international molybdenum isotope measurement standard and data representation. Geostand. Geoanal. Res. 38, 149–151.
Nakagawa, Y., Takano, S., Lutfi Firdaus, M., Norisuye, K., Hirata, T., Vance, D., Sohrin, Y., 2012. The molybdenum isotopic composition of the modern ocean. Geochem. J. 46, 131–141.
Nanne, J.A.M., Millet, M-A., Burton, K.W., Dale, C.W., Nowell, G.M., Williams, H.M., 2017. High precision osmium stable isotope measurements by double spike MC-ICP-MS and N-TIMS. J. Anal. At. Spectrom. 32, 749–765.
Neubert, N., Nägler, T.F., Böttcher, M.E., 2008. Sulfidity controls molybdenum isotope fractionation into euxinic sediments: evidence from the modern Black Sea. Geology 36, 775–778.
Noordmann, J., Weyer, S., Montoyo-Pina, C., Dellwig, O., Neubert, N., Eckert, S., Paetzel, M., Böttcher, M.E., 2015. Uranium and molybdenum isotope systematics in modern euxinic basins: case studies from the central Baltic Sea and the Kylaren fjord (Norway). Chem. Geol. 396, 182–195.
Nunes, F., Norris, R.D., 2006. Abrupt reversal in ocean overturning during the Palaeocene/Eocene warm period. Nature 439, 60–63.
Olivarez-Lyle, A., Lyle, M.W., 2006. Missing organic carbon in Eocene marine sediments: is metabolism the biological feedback that maintains end-member climates? Paleoceanogr. Paleoclimatol. 21. https://doi.org/10.1029/2005PA001230.
Oschlies, A., Brandt, P., Stramma, L., Schmidtko, S., 2018. Drivers and mechanisms of ocean deoxygenation. Nat. Geosci. 11, 467–473.
Pearce, C.R., Cohen, A.S., Parkinson, I.J., 2010. Quantitative separation of molybdenum and rhenium from geological materials for isotopic determination by MC-ICP-MS. Geostand. Geoanal. Res. 33, 219–229.
Pearson, P.N., Foster, G.L., Wade, B.S., 2009. Atmospheric carbon dioxide through the Eocene–Oligocene climate transition. Nature 461, 1110–1113.
Pearson, P.N., McMillan, I.K., Wade, B.S., Dunkley Jones, T., Coxall, H.K., Bown, P.R., Lear, C.H., 2008. Extinction and environmental change across the Eocene–Oligocene boundary in Tanzania. Geology 36, 179–182.
Poulton, S.W., Canfield, D.E., 2005. Development of a sequential extraction procedure for iron: implications for iron partitioning in continentally derived particulates. Chem. Geol. 214, 209–221.
Poulton, S.W., Henkel, S., März, C., Urquhart, H., Flögel, S., Kasten, S., Sinninghe Damste, J.S., Wagner, T., 2015. Continental-weathering control on orbitally driven redox-nutrient cycling during Cretaceous Oceanic Anoxic Event 2. Geology 43, 963–966.
Raiswell, R., Hardisty, D.S., Lyons, T.W., Canfield, D.E., Owens, J.D., Planavsky, N.J., Poulton, S.W., Reinhard, C.T., 2018. The iron paleoredox proxies: a guide to the pitfalls, problems and proper practice. Am. J. Sci. 318, 491–526.
Ravizza, G., Paquay, F., 2008. Os isotope chemostratigraphy applied to organic-rich marine sediments from the Eocene–Oligocene transition on the West African margin (ODP Site 959). Paleoceanogr. Paleoclimatol. 23, PA2204. https://doi.org/10.1029/2007PA001460.
Ravizza, G., Peucker-Ehrenbrink, B., 2003. The marine $^{187}Os/^{188}Os$ record of the Eocene–Oligocene transition: the interplay of weathering and glaciation. Earth Planet. Sci. Lett. 210, 151–165.
Rögl, F., 1999. Mediterranean and Paratethys: facts and hypotheses of an Oligocene to Miocene paleogeography (short overview). Geol. Carpath. 50, 339–349.
Rudnick, R.L., Gao, S., 2003. Composition of the continental crust. In: Heinrich, D.H., Karl, K.T. (Eds.), Treatise on Geochemistry. Pergamon, Oxford, UK, pp. 1–64.
Schulz, H-M., Bechtel, A., Sachsenhofer, R.F., 2005. The birth of the Paratethys during the Early Oligocene: from Tethys to an ancient Black Sea analogue? Glob. Planet. Change 49, 163–176.
Schulz, H-M., Sachsenhofer, R.F., Bechtel, A., Polesny, H., Wagner, L., 2002. The origin of hydrocarbon source rocks in the Austrian Molasse Basin (Eocene–Oligocene transition). Mar. Pet. Geol. 19, 683–709.
Sexton, P.F., Norris, R.D., Wilson, P.A., Pälike, H., Westerhold, T., Röhl, U., Bolton, C.T., Gibbs, S., 2011. Eocene global warming events driven by ventilation of oceanic dissolved organic carbon. Nature 471, 349–352.
Sexton, P.F., Wilson, P.A., Norris, R.D., 2006. Testing the Cenozoic multisite composite 18O and ^{13}C curves: new monospecific Eocene records from a single locality, Demerara Rise (Ocean Drilling Program Leg 207). Paleoceanogr. Paleoclimatol. 21. https://doi.org/10.1029/2005PA001253.
Sissingh, W., 1997. Tectonostratigraphy of the North Alpine Foreland Basin: correlation of Tertiary depositional cycle and orogenic phases. Tectonophysics 282, 223–256.
Tessin, A., Chappaz, A., Hendy, I., Sheldon, N., 2019. Molybdenum speciation as a paleo-redox proxy: a case study from Late Cretaceous Western Interior Seaway black shales. Geology 47, 59–62.
Tissot, F.L.H., Dauphas, N., 2015. Uranium isotopic compositions of the crust and ocean: age corrections, U budget and global extent of modern anoxia. Geochim. Cosmochim. Acta 167, 113–143.
Veto, I., 1987. An Oligocene sink for organic carbon: upwelling in the Paratethys? Palaeogeogr. Palaeoclimatol. Palaeoecol. 60, 143–153.
Vorlicek, T., Helz, G.R., Chappaz, A., Vue, P., Vezina, A., Hunter, W., 2019. Molybdenum burial mechanism in sulfidic sediments: iron-sulfide pathway. ACS Earth Space Chem. 2, 565–576.
Wade, B.S., Pearson, P.N., 2008. Planktonic foraminferal turnover, diversity fluctuations and geochemical signals across the Eocene/Oligocene boundary in Tanzania. Mar. Micropaleontol. 68, 244–255.
Wagner, L.R., 1998. Tectono-stratigraphy and hydrocarbons in the Molasse Foredeep of Salzburg, Upper and Lower Austria. In: Mascle, A., Puigdefàbregas, C., Luterbacher, H.P., Fernàndez, M. (Eds.), Cenozoic Foreland Basins or Western Europe. In: Geological Society Special Publications, vol. 134, pp. 339–369.
Wang, X., Planavsky, N.J., Reinhard, C.T., Hein, J.R., Johnson, T.M., 2016. A Cenozoic seawater redox record derived from $^{238}U/^{235}U$ in ferromanganese crusts. Am. J. Sci. 316, 64–83.
Weiss, R.F., 1970. The solubility of nitrogen, oxygen and argon in water and seawater. Deep-Sea Res. 17, 721–735.
Zachos, J.C., Dickens, G.R., Zeebe, R.E., 2008. An early Cenozoic perspective on greenhouse warming and carbon-cycle dynamics. Nature 451, 279–283.